Appl. Phys. A 76, 653–664 (2003)
DOI: 10.1007/s00339-002-2010-7

C. TEICHERT

Self-organized semiconductor surfaces as templates for nanostructured magnetic thin films

Institut für Physik, Montanuniversität Leoben, Franz Josef Str. 18, 8700 Leoben, Austria

Received: 31 July 2002/Accepted: 2 October 2002
Published online: 5 February 2003 • **© Springer-Verlag 2003**

ABSTRACT Spontaneous pattern formation during epitaxial growth or ion erosion of semiconductor wafers offers an elegant route towards large-area nanostructured surfaces. In homoepitaxy, kinetics may result in rather uniform three-dimensional islands. In the case of semiconductor heteroepitaxy, strain relief leads to the formation of nanofaceted three-dimensional crystallites, which may self-organize into quasiperiodic arrays. By tuning substrate miscut and film thickness, or growing superlattices, a variety of patterns with different symmetries can be obtained, as will be summarized for the model system of SiGe on Si(001). Since these self-organized nanostructure arrays cover the entire wafer on which they are grown, they can serve as large-area nanopatterned substrates for subsequent deposition of magnetic thin films. It will be demonstrated that such templates allow the study of correlations between magnetic and chemical interfacial roughness, as well as the influence of pattern symmetry on the magnetic anisotropy of thin Co films. Furthermore, shadow deposition of magnetic material onto specially faceted nanostructure arrays allows the fabrication of nanomagnet arrays and the study of their magnetic properties.

PACS 68.55-a; 68.37.Ps; 75.70.-i; 75.75.+a

1 Introduction

The search for efficient fabrication techniques for nanostructured surfaces is an important issue within the field of nanotechnology since, due to decreasing structure sizes, the "top-down" approach using lithography techniques becomes more and more expensive. Currently, there are two alternative approaches towards nanostructured surfaces under consideration. The first is based on modern scanning-probe-microscopy (SPM) techniques such as scanning tunnelling microscopy (STM) or atomic-force microscopy (AFM), where nanostructures are achieved by either manipulating single atoms [1] or by using the probe as a stylus or pen to "write" structures with dimensions of a few tens of nanometers [2]. The considerable time exposure of these methods can be overcome by operating more than one probe in parallel. The successful implementation of a 32×32 tip array [3] has to be considered as a very promising step towards efficient SPM-based nanostructure fabrication. The second – rather elegant – approach is the concept of nanostructure formation by self-organization, where atoms or molecules spontaneously arrange in rather uniform aggregates forming large-area nanopatterns. This "bottom-up" phenomenon can be observed at surface reactions [4], during epitaxial growth [5, 6], and even in erosion of surfaces by ion bombardment [7]. The resulting patterns can be divided into one-dimensional (1D) ripple structures and two-dimensional (2D) nanostructure arrays, as is sketched in Fig. 1 for the case of epitaxial growth. Although self-organized nanostructure formation occurs also on metal and insulator surfaces, at present semiconductor substrates (especially silicon) are advantageous because of their superior quality, large size and long-term stability. In particular, the widely and intensively studied strained-layer semiconductor heteroepitaxy can be regarded as a model system for nanostructure self-organization on solid surfaces [8, 9]. Here, large-area arrays of rather regular and uniform nanostructures are obtained simply by growing semiconductor thin films under appropriate conditions. The self-organization approach has the disadvantage of having less control on structure, size and shape of the nanostructures compared to man-made structuring. However, for nanotechnology applications where uniformity of structures has priority over special size and shape requirements, this concept promises to become a cost-efficient route towards large-scale arrays of nanostructures. A prominent example is the utilization of self-organized quantum dots for optoelectronic applications [10]. A second potential application results from the fact that these nanostructure arrays

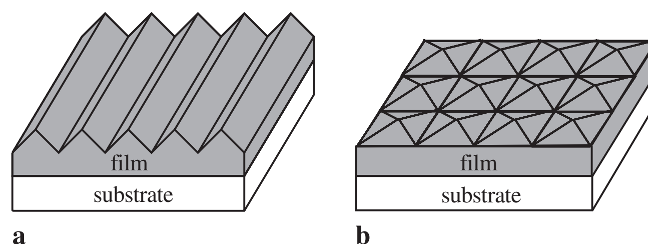

FIGURE 1 Schematic presentations for spontaneous pattern formation in epitaxial growth: **a** 1D ripple pattern due to bunching of preexisting substrate steps. **b** 2D array of faceted crystallites

✉ Fax: +43-3842/402-760, E-mail: teichert@unileoben.ac.at

cover the area of the entire semiconductor wafer – for silicon up to 300 mm in diameter – on which they are grown. Thus, they can serve as large-area nanopatterned templates for subsequent deposition of various materials. Depositing magnetic material onto these templates gives easy access to nanostructured magnetic thin films and in conjunction with the technique of shadow deposition even nanomagnet arrays can be efficiently created [11]. Thus, the combination of self-organized semiconductor surfaces and thin-film magnetism represents an interesting variant within the broad efforts of fabricating magnetic nanostructures [12–14] for future data-storage applications.

Here, we will first review the different routes towards self-organized semiconductor nanostructure arrays. The broad spectrum of possible nanopatterns obtained in strain driven self-organization will be exemplified for Stranski–Krastanov growth of SiGe alloy layers on the technologically relevant Si(001) surface. Nanostructure formation in semiconductor homoepitaxy and under ion erosion will be briefly illustrated for Si/Si(001) growth and Ar^+ ion bombardment of GaSb(001), respectively. In the second part, it will be demonstrated how self-organized patterns can serve as templates to efficiently fabricate various nanostructured magnetic thin films. Examples are presented for the influence of pattern geometry on magnetic roughness and magnetic anisotropy. Finally, the fabrication of large-area nanomagnet arrays by grazing-incidence deposition of Co onto a specially nanofaceted SiGe covered Si template is demonstrated.

2 Experimental

The SiGe single films and the SiGe/Si superlattices presented here have been grown by solid-source molecular beam epitaxy (MBE) on 4-inch vicinal Si(001) wafers, with the substrate mostly kept at 550 °C. For the details of substrate vicinality, growth conditions and sample structures the reader is referred to [15]. The GaSb(100) sample was bombarded with 500-eV Ar^+ ions under normal incidence with an ion current density of about 5×10^{16} cm^{-2} [7]. During ion sputtering, the substrate temperature was kept below 100 °C by water cooling. The surface morphologies of the semiconductor templates have been investigated with a Digital Instruments MultiMode AFM under ambient conditions. For each image presented, the color-scale range is given with bright corresponding to higher surface features. For the shallow SiGe nanostructures, conventional Si_3N_4 tips and sharpened Si tips were sufficient to obtain high-resolution images. In order to provide high spatial resolution of the ion-bombarded sample, plasma-sharpened high-density carbon (HDC) tips as well as carbon nanotube (CNT) tips with an opening angle less than 4° and tip radius of ≤ 5 nm have been used. Integral information on nanostructure arrangement and their three-dimensional (3D) shape has been obtained by analyzing 2D power spectra and histograms of orientations of the local surface normals calculated from the AFM topographs.

On the native-oxide-covered self-organized SiGe films, thin Co films were grown by dc magnetron sputtering [16] or by pulsed-laser deposition (PLD) [11]. To avoid cobalt silicide formation and oxidation of Co, the film was embedded between two Cu films. To ensure long-term stability, these sandwiches were finally capped with an Au film [11] or a passivating Al layer [16]. Figure 2 shows the general sample composition and illustrates the deposition geometries for normal incidence and shadow deposition. Growth was performed under conditions that ensured smooth films [16, 17]. For normal incidence (Fig. 2b), this results in continuous films that coherently cover the self-organized templates, as has been verified by AFM. Under appropriate grazing incidence conditions only selected facet types are exposed to the particle beam (Fig. 2c), resulting in an array of separated Co nanostructures. Longitudinal magneto-optic Kerr effect (MOKE) measurements were recorded as a function of the azimuthal sample orientation to reveal possible anisotropies in the in-plane magnetization of the continuous films and the nanomagnets. To study the structural and magnetic roughness of the continuous Co films, diffuse X-ray resonant magnetic scattering (DXRMS) measurements were performed using circularly polarized X-rays tuned to the L_3 absorption edge of Co ($E = 775$ eV) [16]. To allow an intensity mapping far out in reciprocal space and to ensure constant-penetration-depth azimuthal transverse scans, $I(\Omega)$ were measured under a fixed angle of incidence ($\theta = 3°$) rather than recording $I(2\theta)$ rocking curves.

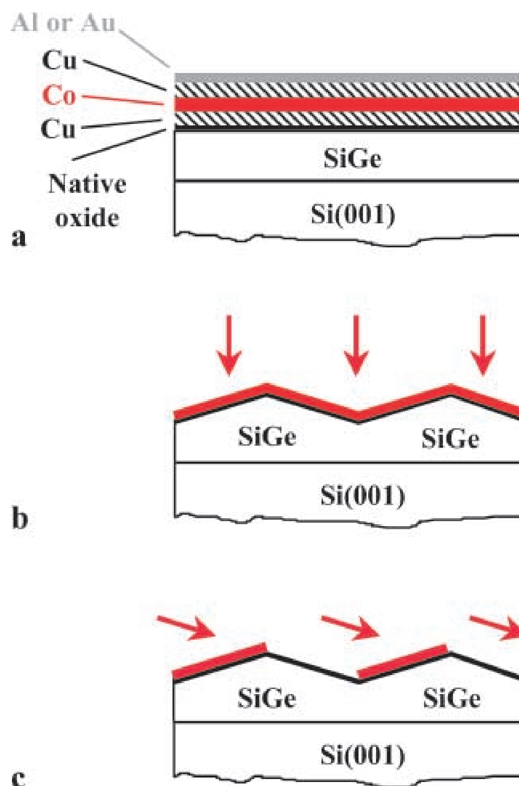

FIGURE 2 Sample structure and deposition conditions for magnetic thin films on semiconductor nanostructures in cross-sectional presentation. **a** General sample structure: On the native oxide of the SiGe film a Cu/Co/Cu sandwich is grown. The final cap layer is either of Al or Au. **b** Normal incidence onto a self-organized semiconductor surface resulting in a continuous magnetic thin film. **c** Shadow deposition by grazing incidence on a nanofaceted semiconductor template resulting in deposition onto selected facets only. The *arrows* represent the direction of incidence

3 Self-organized semiconductor nanostructures

3.1 *Pattern formation in heteroepitaxy*

In the presence of lattice mismatch, strain builds up during heteroepitaxial growth because the film starts to grow with the lattice constant of the substrate. As a consequence, the growth is influenced by elastic and plastic strain-relaxation mechanisms. For the case of compressive strain – as for Ge/Si growth, where the Ge lattice constant is 4.2% larger than that of Si – the resulting stages of strain relief are illustrated in Fig. 3. The first stage is the growth of a uniformly strained wetting layer, consisting of one or several monatomic layers where strain is partly vertically relieved by tetragonal distortion (Fig. 3a). In addition, lateral strain relief can occur, resulting in surface reconstruction. Nevertheless, the elastic energy increases in this uniformly strained wetting layer with film thickness. Thus, at a certain number of smooth layers, the film may become unstable against a long-wavelength corrugation of the surface, the so-called Asaro–Tiller–Grinfeld instability [18], and finally 3D islands (crystallites) are formed. The latter situation corresponds to the Stranski–Krastanov growth in the thermodynamic classification of growth modes [19]. The crystallites that form initially are coherently strained (Fig. 3b) [20]. The increase of surface energy is overcompensated by a decrease of strain energy due to elastic strain relaxation towards the bulk lattice constant in the upper parts of the crystallites. If this mechanism is no longer sufficient to relieve strain, plastic strain relief sets in by introducing misfit dislocations at the film/substrate interface. This results in dislocated crystallites that are fully relaxed at the top, i.e. having the bulk lattice constant of the film material (Fig. 3c). In principle, in all three stages formation of self-organized surface patterns can be observed. However, the scheme presented in Fig. 3 is very general and has to be modified whenever considering a particular growth system.

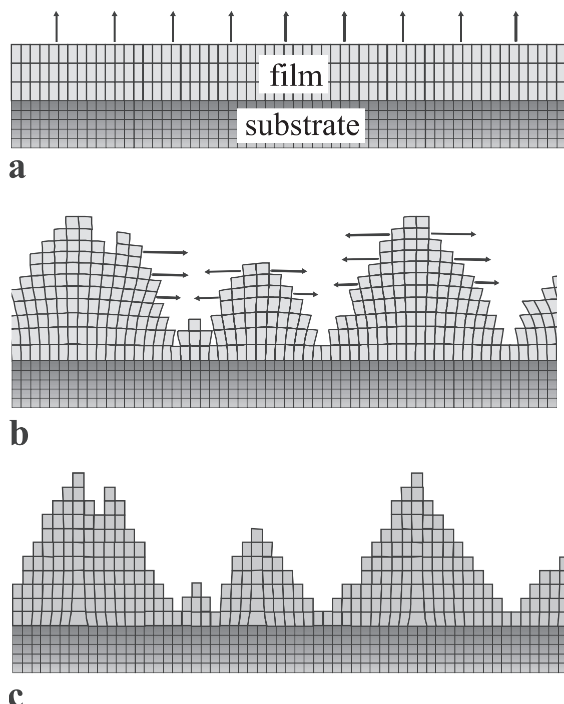

FIGURE 3 General scenario of strain relief in heteroepitaxy for the case that the lattice constant of the film exceeds that of the substrate. **a** Pseudomorphic growth of tetragonally distorted wetting layer. **b** Formation of coherently strained 3D islands. The *arrows* indicate the direction of elastic strain relief. **c** Strain relaxation by introduction of misfit dislocations in the 3D islands

For solid-source MBE of pure Ge films or $Si_{1-x}Ge_x$ alloys on Si(001), the following sequence of strain relief mechanisms has been established [15]. Here, emphasis will be on the morphological properties. For a detailed discussion on the underlying mechanisms the reader is referred to a recent review [9].

The first stage of strain relief in $Si_{1-x}Ge_x$/Si(001) is the formation of a $(2 \times n)$ surface reconstruction [21–23]. There, about every 9th dimer is missing in the dimer rows of the original Si(001) - 2×1 reconstruction. The resulting dimer vacancies, which allow lateral strain relief, self-organize into well-ordered rows [24]. In a second stage, ripple formation by step-bunching of the pre-existing steps of the vicinal Si(001) substrate is observed [25] where the ripple distance can be tailored by varying the polar miscut angle of the substrate [15, 26]. The ripples have a symmetric triangular cross-section and consist of an extended (001) terrace on the one side and a step bunch with doubled step density compared to that of the substrate on the other side [15]. Originally, this effect has been explained solely by a strain-driven phenomenon [27]. Recently, it has been shown for polar miscut angles less than 1° that the step bunching occurs in the Si buffer layers commonly grown prior to Ge deposition [28, 29], and is mainly due to a kinetic growth instability [30]. For polar substrate miscuts of 2°, however, the kinetically induced buffer layer morphology does not show ripples at the employed growth temperature [31], whereas the subsequently grown SiGe films do show a rippled morphology [9, 26]. Thus, for large miscut substrates we have to assume a significant strain-driven contribution to the observed ripples. Figure 4 shows such a rippled morphology for a 2.5-nm $Si_{0.55}Ge_{0.45}$ film grown on a Si(001) substrate with a 2° miscut towards [100]. The corresponding 2D power spectrum (inset of Fig. 4a) exhibits a clear split peak. From its position and its width, a predominant ripple spacing of 72 ± 10 nm is determined. The average height of the ripples is about 1.5 nm, as can be seen from Fig. 4b.

In a third stage, coherently strained SiGe crystallites form, which are bounded by {105} facets [32]. The characteristic of the Ge(105) face is that it has a strained rebonded step structure, as found recently [33]. In a single SiGe film grown under the conditions used here, their base shape is predominantly rectangular, resulting in a "hut" shape [32]. They form an interlocked array with a broad size and shape distribution [34, 35]. Uniformity of size and shape improves a lot when growing a SiGe/Si superlattice [34]. This is demonstrated in Fig. 5, showing the 20th alloy layer of a $20 \times$ (2.5-nm $Si_{0.25}Ge_{0.75}$/10-nm Si) multilayer stack. The morphology is dominated by rather uniform four-sided {105}-faceted pyramids that tend to arrange in a close-packed square array (Fig. 5b). Thus, the entire surface is covered by the {105} facets, which are tilted 11.3° with respect to the (001) surface. The resulting 2D power spectrum shows four narrow peaks and even second-order peaks, indicating the high degree of unifor-

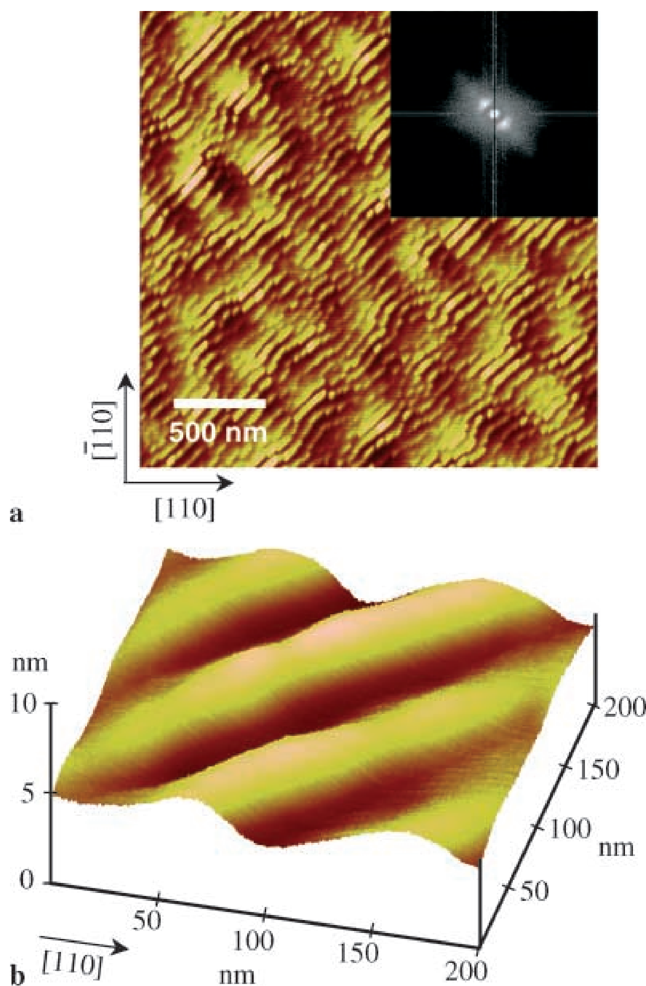

FIGURE 4 Step-bunched ripple formation in SiGe films grown on large-miscut Si(001) substrates. **a** 2.5 μm × 2.5 μm AFM image of a 2.5 nm $Si_{0.55}Ge_{0.45}$ film grown on a Si(001) misoriented 2° towards [100], color scale range: 5 nm. The *inset* shows the corresponding 2D power spectrum. **b** Three-dimensional AFM image to emphasize the shallow ridge structure of the ripples with slopes of about 2° with respect to the nominal surface. Please note that the *vertical scale* is exaggerated by a factor of about 8

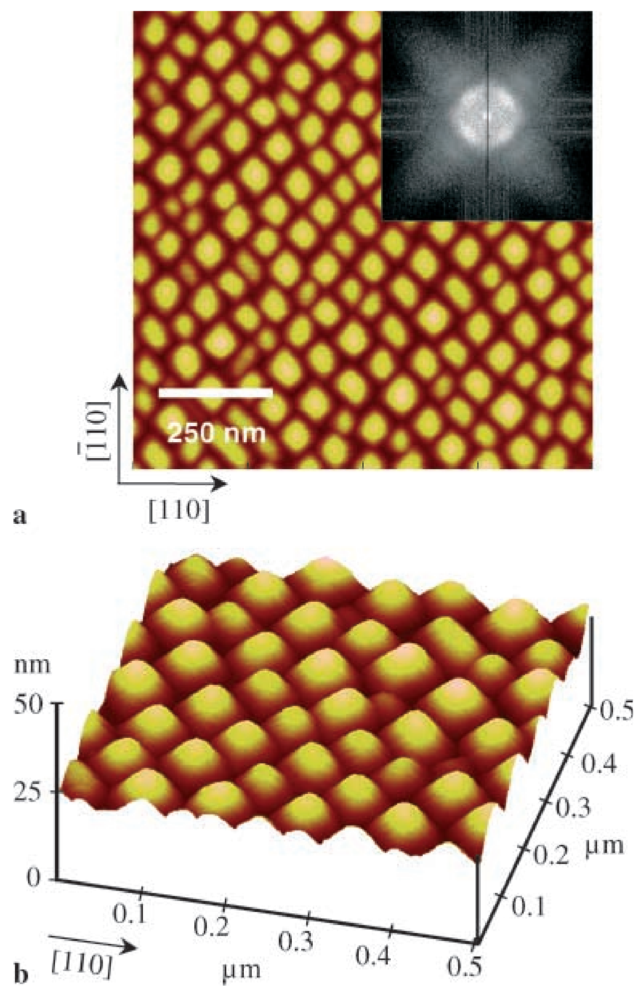

FIGURE 5 Strain mediated self-organization of {105} facetted SiGe crystallites in a SiGe/Si superlattice grown on Si(001). **a** 1 μm × 1 μm AFM image of the 20th alloy layer of a 20 × (2.5 nm $Si_{0.25}Ge_{0.75}$/10 nm Si) multilayer film, color scale range: 20 nm. The *inset* shows the 2D power spectrum calculated from a 5 μm × 5 μm image. **b** 3D AFM image to emphasize the laterally close-packed array of the four-sided SiGe pyramids. Please note that the *vertical scale* is exaggerated by a factor of about 4

mity present. From quantitative analysis of the 2D power spectra [15, 34] an average of 85 ± 12.5 nm has been obtained for the edge length of the pyramid bases, resulting in an average pyramid height of 8.5 ± 1.3 nm. The observed self-organization is due to strain mediation through the Si spacer layers causing not only a lateral but also a 3D self-organization of the crystallites with vertical stacking in the superlattice [36]. This effect is rather general and has also been observed in III–V semiconductor superlattices (see for example [37]). In the case of a strong elastic anisotropy of the spacer layer, as for the IV–VI superlattices $PbSe/Pb_{1-x}Eu_xTe$ grown on PbTe, deviations from the vertical stacking can be observed [38, 39].

It should be noted that ordering of {105} crystallites can also be achieved in single layers. For example, when growing a 2.5-nm $Si_{0.25}Ge_{0.25}$ film on a substrate with 2° polar miscut towards [100], as used for the sample presented in Fig. 4, the ripple structure guides the later-evolving {105} "hut" crystallites into chains with a very narrow distribution of their base width [15, 26].

At the next stage of strain relief, 3D crystallites with facets steeper than {105} arise, allowing the islands to grow larger, resulting in multifaceted "dome" crystallites [40]. The facets that have been observed are {113} (tilt angle 25.2°) [41], {102} (26.6° tilt angle) [40], {15 3 23} (tilt angle 33.6°) [41, 42]. Finally, the islands have (001) terraces on top, resulting in mesa structures. In the dome stage, where the shape and size distribution of the crystallites is rather broad, to our knowledge no arrangement into a self-organized pattern has been observed so far.

With the steeper facets evolving, plastic strain relief sets in by the formation of misfit dislocations (for a review see [43]). Misfit dislocations in Ge and SiGe on Si(001) are 60° dislocations that glide on a {11$\bar{1}$} plane. They manifest themselves at the surface by ridges and troughs [41] that are extended in either [110] or [$\bar{1}$10] directions. At a sufficiently high density of dislocations, a misfit dislocation network occurs at the substrate/film interface that manifests at the surface as a so-called "cross-hatch" pattern [41]. The pattern is characterized by a network of very straight ridges

and troughs along ⟨110⟩, which may extend over several tens of micrometers. Under certain preparation conditions, pyramidal {105}-faceted islands align in ⟨110⟩ directions and decorate in this way the misfit dislocations [44]. This preferential nucleation of pyramid-like islands on top of misfit dislocations has been utilized to create regular island arrays that are guided by an underlying network of misfit dislocations, which has been created by rather complex growth procedures [45, 46]. However, the resulting crystallite density is small. A simple technological way is a two-stage growth process originally dedicated to fabricating strain-relaxed SiGe virtual substrates [47]. There, the SiGe growth is started at low growth temperatures, just above the amorphization temperature. In the second stage, growth proceeds at 550 °C, the usual growth temperature. The dislocation network and the {105}-faceted islands form simultaneously when increasing the growth temperature. This interplay of dislocation-network evolution and crystallite formation results in chains of pyramidal crystallites that are very straight and extend over tens of micrometers [48]. By applying ion-assisted MBE [49], the density of the crystallite chains can be increased to a close-packed chain array [48]. This is demonstrated in Fig. 6, which shows an 80-nm $Si_{0.7}Ge_{0.3}$ alloy film of which the first 30 nm have been grown under simultaneous 1 keV Si^+-ion bombardment at 150 °C. The morphology is clearly dominated by a dense crosshatch pattern that is decorated by uniform pyramid-like islands. The periodicity of these crystallites in the ⟨110⟩ directions is about 190 nm, as obtained from the 2D power spectrum (inset of Fig. 6a). Only a few small areas exhibit an interlocked array of disordered hut crystallites. In the dense dislocation areas, however, we observe a surprisingly uniform surface pattern (Fig. 6b) that looks like a man-made structure rather than a spontaneously formed one. The pattern is best described by a checkerboard array of four-sided pyramids and pits. The histogram of orientations of local surface normals reveals that the pattern consists of {105} facets, which have a rhombic shape that deviates only slightly from a square (acute angle of 88.9°). The edge length of the rhombs is about 95 nm [9].

The driving force for this pattern is assumed to originate again in the special elastic properties of the Ge{105} facet. Optimizing the growth conditions, we expect to increase the areas of perfect order from about 1 µm (now) to several tens of micrometers. For a fixed Ge concentration and therefore fixed lattice misfit, we could not change the periodicity of the pattern and thereby the size of the nanofacets. First attempts using tuneable dislocation networks by twist wafer bonding [50] resulted in significantly smaller crystallite sizes which, however, lacked the uniformity obtained here.

The selection of self-organized SiGe nanopatterns presented in Figs. 4 – 6 already demonstrates a surprising diversity in pattern geometry, and structure size and shape, which is obtained by utilizing the strain-relief mechanism in one particular heteroepitaxial system (for more variations see [9, 15]). These mechanisms have been found to occur also in III–VI, II–VI, and IV–VI heteroepitaxial systems, resulting in similar patterns where the structure size, facet orientation, etc. is determined by the particular growth system. Because of the large parameter set (which can be even increased by dynamic variation of growth conditions), a further improvement of ordering as well as an abundance of novel self-organized patterns in semiconductor heteroepitaxy is expected.

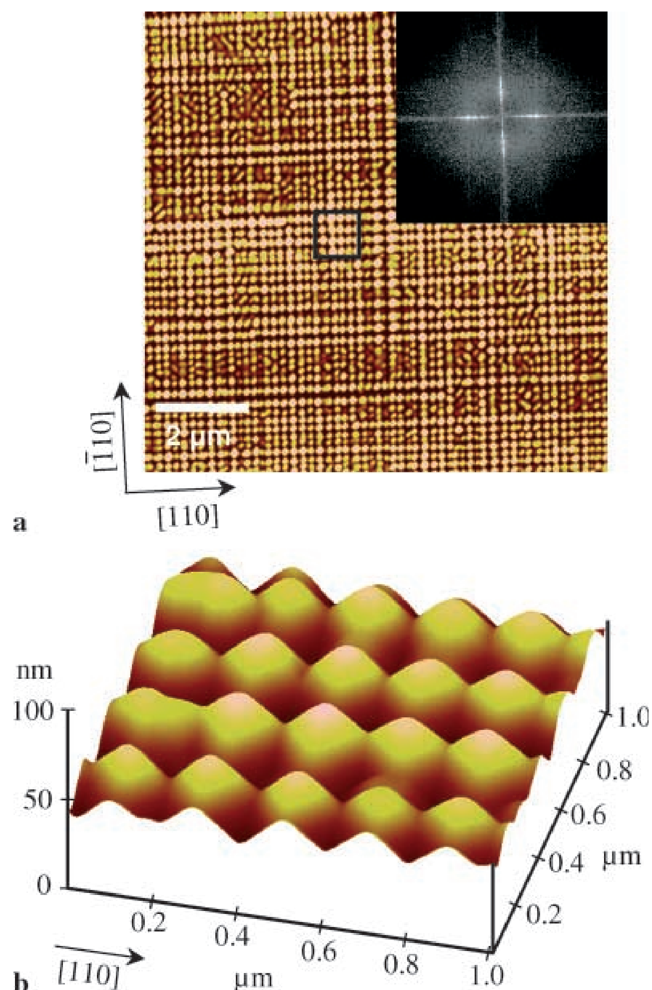

FIGURE 6 Regular nanofacet array due to the interplay of a dislocation network and island formation. **a** 10 µm × 10 µm image of an 80 nm $Si_{0.7}Ge_{0.3}$ film grown in a two-stage process (see text) on Si(001), color scale range: 15 nm, *inset*: 2D power spectrum calculated from a 20 µm × 20 µm image. **b** 3D AFM image of the area with a dense dislocation network framed in **a** showing a checkerboard array of {105} faceted pyramids and pits. The *vertical scale* is exaggerated by a factor of about 4

3.2 *Nanostructure formation in homoepitaxy*

For a long time, efforts in semiconductor homoepitaxy were focused on understanding atomic processes in the early growth stages and on the fabrication of high-quality smooth buffer layers (for recent reviews of these efforts on Si surfaces see [51, 52]). To ensure smooth growth fronts, low miscut substrates (a few tenths of a degree) are used and growth conditions are chosen that enable step-flow growth, where the growth front is copied from layer to layer. However, also in semiconductor homoepitaxy, 1D and 2D nanostructure arrays can be achieved. As already mentioned in Sect. 3.1, it has recently been clarified that in certain temperature ranges kinetic growth instabilities cause 1D ripple arrays in Si/Si(001) homoepitaxy [28, 30]. By exploring the growth at slightly higher miscut (1–2° with respect to Si(001)), the

formation of 2D-like zigzag patterns has been observed [31]. Since these growth structures also exhibit a surprising uniformity, Si homoepitaxy on vicinal substrates offers another route – even simpler than heteroepitaxial growth – for fabricating nanostructured self-organized surfaces.

A promising example is presented in Fig. 7, which shows the surface morphology of a 10-nm Si film grown by chemical vapour deposition on a vicinal Si(001) substrate with a 4° miscut towards [110] (for details see Sect. 2.2 of [9]). As one can see from the large-scale image (Fig. 7a), there are 3D crystallites with preferential base edges along the close-packed ⟨110⟩ direction. The arrangement of the crystallites on the surface is isotropic, as is reflected in the ring structure of the corresponding power spectrum (labelled A in the inset of Fig. 7a). From the radius of the ring (dashed line) the preferential separation of the crystallites of 280 nm is deduced. The high-resolution AFM image presented in Fig. 7b (especially when looking at the rims of the image) reveals a mesa-like shape for the crystallites. Analysis of the histogram of the orientations of local surface normals [9, 41] reveals a (001) terrace on top (tilted by 4° with respect to the nominal surface) and the existence of {113} facets tilted 25.2° with respect to (001). The average edge length of these terraces (determined from the position of the peak marked B in the 2D power spectrum) is about 140 nm. To account for the substrate miscut, the () facets are larger than the (113), as is seen in the image rim along [110]. According to the facet analysis, there are shallow {117} facets inserted (11.4° tilt angle), resulting in a less abrupt transition from {113} to (001). The mean height of these multifaceted crystallites is about 15 nm [9].

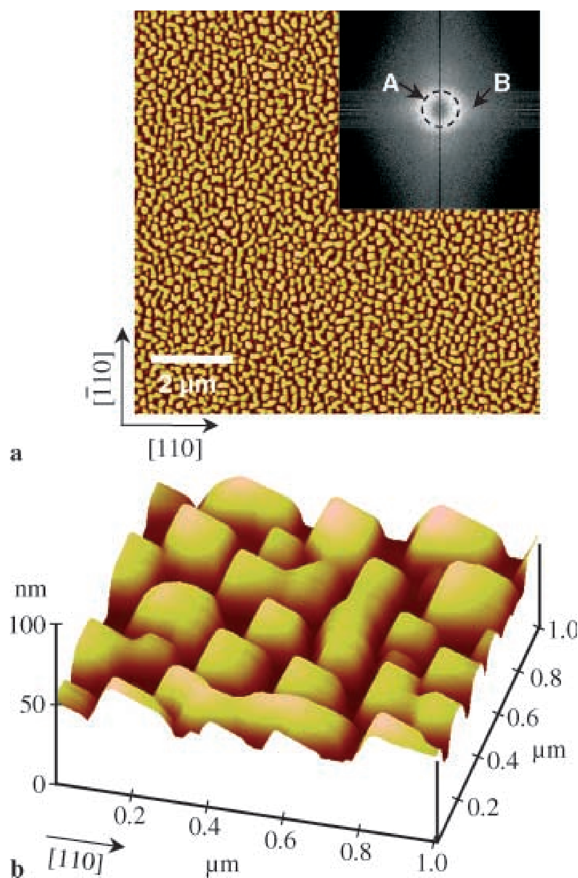

FIGURE 7 Uniform multifaceted crystallites in homoepitaxy on vicinal Si(001) substrates. **a** 10 µm × 10 µm image of a 10 nm Si film grown by chemical vapor deposition on Si(001) misoriented 4° towards [110], color scale range: 15 nm, *inset*: corresponding 2D power spectrum. **b** 3D AFM image revealing the mesa shape of the crystallites. The *vertical scale* is exaggerated by a factor of about 4. The ring in the 2D power spectrum marked A originates from the isotropic arrangement of the islands whereas the four spots (B) reflect the size of (001) tops of the mesas

3.3 *Ion-bombardment-induced self organization*

It is well known that ion bombardment of solid surfaces causes surface roughening, which is fully undesired in applying ion sputtering for surface cleaning or layer removal. However, it has also been known for quite a time that ion erosion may result in microscopic self-organized 1D and 2D surface patterns [53] similar to the ones sketched in Fig. 1 for epitaxial growth. Initiated by modern SPM techniques, this phenomenon is now intensively explored on the nanometer scale because it also bears the potential for large-scale nanostructuring of solid surfaces. Ripple formation has been found under oblique ion incidence for both metal surfaces [54] and semiconductor surfaces [55]. It is explained by a competition of curvature-dependent sputtering yield and surface-diffusion-induced smoothing [56]. Bombardment-induced 2D nanostructures are frequently observed on fcc single-crystal metal surfaces, where the shape of the structures is significantly determined by surface geometry and the kinetics of surface diffusion [57–61]. However, for semiconductor surfaces, it took until 1999 to discover ion-bombardment-induced 2D nanostructure arrays [7]. For low-energy Ar^+-ion bombardment of GaSb(001) under normal incidence, a hexagonally ordered "dot" pattern evolved from an initially flat surface. Figure 8 shows high-resolution AFM images of this self-organized morphology, obtained after 500-eV Ar^+-ion bombardment [62]. The 2 µm × 2 µm image (Fig. 8a) reveals domains of hexagonally close-packed dot arrays with a lateral dimension ≤ 0.5 µm. Due to the random azimuthal orientation of these domains, a ring-like power spectrum is observed. The high degree of self-organization is evident by the appearance of up to four orders of this ring structure. From the radius of the inner ring and its width, an average dot diameter of 43 nm ± 10% has been determined [62]. Figure 8b presents an AFM topograph in 3D presentation, recorded with a carbon nanotube tip, allowing us to resolve tilt angles in the depressions between the dots up to 80°. Line scans through the centers of the 20–25-nm high dots have almost a semi-spherical shape with a continuously changing slope, indicating that the 3D dot shape is a spherical calotte rather than a cone. The fact of a non-faceted dot shape is supported by the observation of a 2-nm-thick amorphous surface layer after ion irradiation [63]. It is worthwhile mentioning that the ordering does not depend on surface orientation. The same pattern has been measured for ion-bombarded GaSb(111) substrates as well as for amorphous GaSb [63]. This fact can also be explained by the surface amorphization. Still, the question remains as to why the ordering is hexagonal. Investigations of the temporal evolution of the pattern showed that the self-organized morphology, once established, is stable for very long sputtering times, and the predicted kinetic roughening

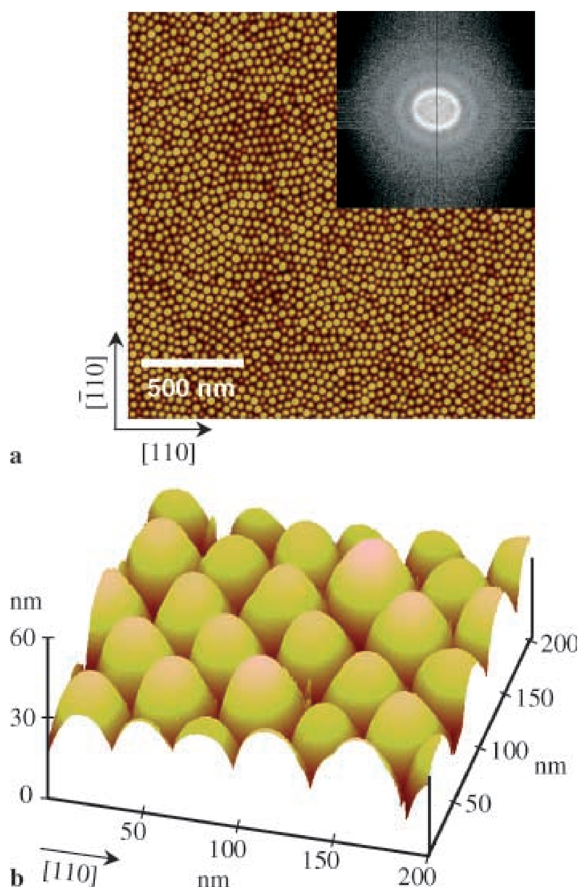

FIGURE 8 Ion bombardment induced hexagonal dot array. **a** 2 μm × 2 μm AFM image of GaSb(001) bombarded with 500 eV Ar^+ under normal incidence for 600 s, color scale range is 50 nm, inset: corresponding 2D power spectrum. **b** 3D AFM topograph recorded with a carbon nanotube AFM tip. It reveals the hemispherical shape of the resulting nanostructures. In contrast to common presentations the vertical scale is not exaggerated

accompanied by a disappearance of the ordering [64] has not yet been observed [62]. It should be noted that the same self-organization effect with very efficient ordering is obtained under oblique ion incidence and simultaneous azimuthal sample rotation [65]. Hexagonal dot patterns are not only found on III–V semiconductors but also on Si(001), however, with a lower degree of ordering [66]. As all these dot patterns have been fabricated at rather low substrate temperatures, resulting in surface amorphization, they exhibit non-faceted nanostructures with rather continuously changing slopes. Therefore, they represent an interesting template class complementing the possibilities offered by the nanofaceted epitaxial patterns (Sect. 3.1 and 3.2).

4 Magnetic thin films on self-organized templates

4.1 *Magnetic roughness*

With decreasing thickness of magnetic thin films used, for example in magnetoelectronic devices, the film interface becomes more and more important. If these films are embedded in non-magnetic material, there are two interfaces: a chemical boundary and a magnetic boundary [67]. The latter is defined by the outermost atoms of the magnetic film that do follow the applied magnetic field. Modern synchrotron radiation facilities now provide the tools to distinguish between both boundaries [68, 69]. This is in particular possible using DXRMS mesurements [16, 70–72]. There, azimuthal transverse scans are recorded using elliptically polarized photons with an energy tuned to an absorption edge of the magnetic material. Scattered intensities $I_+(\Omega)$ and $I_-(\Omega)$ are measured with the photon helicity parallel (+) or antiparallel (−) to the film magnetization $\boldsymbol{M}$. The average intensity $I_{\text{ave}}(\Omega) = 1/2(I_+ - I_-)$ corresponds to the charge scattering and reflects the chemical roughness. The difference $\Delta I(\boldsymbol{M}, \Omega) = I_+(\Omega) - I_-(\Omega)$ is element specific. It was first identified as purely magnetic scattering, however, a subsequently developed theory identified $\Delta I(\boldsymbol{M}, \Omega)$ as a cross-correlation of charge and magnetic scattering [73]. The diffuse components of $I_{\text{ave}}(\Omega)$ and $\Delta I(\boldsymbol{M}, \Omega)$ can be analyzed in terms of the rms roughness σ, the lateral correlation length ξ, and the roughness exponent α [9, 16]. The detailed theoretical formalism for the interpretation of DXRMS measurements given in [73] allows us to extract the roughness parameters of the pure magnetic roughness. However, below we will restrict ourselves to a qualitative interpretation of the results.

In one of the early studies of magnetic roughness using DXRMS, magnetic thin films grown on self-organized semiconductor templates have already been included [16]. The results are summarized in Fig. 9 (for details see [9, 16]), which shows $\Delta I(\boldsymbol{M}, \Omega)$ and $I(\Omega)_{\text{ave}}$ transverse scans for 2-nm Al/2-nm Co/1-nm Cu/2-nm Co sandwiches deposited onto a smooth Si(001) wafer (Fig. 9a) and a Si(001) substrate covered by an alloy-terminated 40 × (2.5 nm $Si_{0.25}Ge_{0.75}$/10 nm Si) multilayer film (Fig. 9b). For each sample, 1 μm×1 μm AFM images of the corresponding sandwich surfaces are also presented. The sandwich grown on a smooth Si(001) wafer has an featureless morphology with a small rms roughness of 0.27 nm. The surface of the sandwich deposited onto the self-organized {105}-faceted pyramids still reveals the morphology of the underlying SiGe template (which is very similar to the one presented in Fig. 5a [35]). The rms value of $\sigma = 3.8$ nm is the same as that for the corresponding SiGe substrate [35]. Thus, one can conclude that the interfacial roughness of all individual films in this sample is dominated by the template morphology. The corresponding DXRMS results are surprisingly different. For the smooth template, the diffuse component of $\Delta I(\boldsymbol{M}, \Omega)$ is significantly smaller and narrower than that of $I(\Omega)_{\text{ave}}$, indicating that the magnetic roughness is smoother but has a larger lateral correlation length than the structural roughness. This behavior is rather general for magnetic thin films deposited onto smooth substrates independent of the fact of whether they are covered by a non-magnetic cap layer [16, 70, 72] or are uncapped [71]. In contrast, for the nanofaceted template (Fig. 9b) $\Delta I(\boldsymbol{M}, \Omega)$ and $I(\Omega)_{\text{ave}}$ are identical (within the uncertainty of the measurement). In other words, in this case the structural and the magnetic boundaries are completely correlated. Because the same was observed for deposition on an interlocked array of non-uniform {105}-faceted hut crystallites [9], we have to assume that the behavior is triggered by the existence of the nanofacets. In Fig. 10, cross-sectional sketches of the upper Al/Co interface are presented to qualitatively explain the different behaviors on a smooth and a nanostructured substrate. The randomly rough film (Fig. 10a) has structural asperities

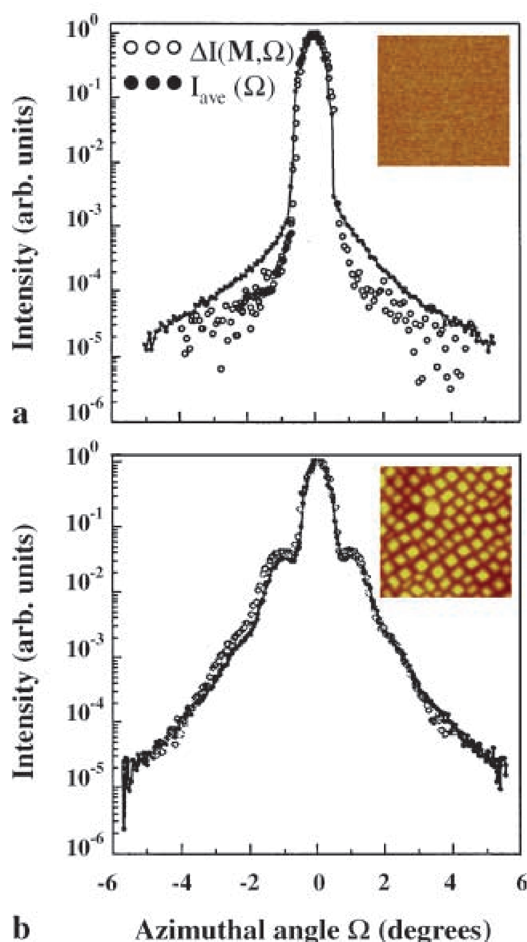

FIGURE 9 $\Delta I(M, \Omega)$ and $I(\Omega)_{ave}$ transverse scans of 2 nm Al/2 nm Co/1 nm Cu/2 nm Co sandwiches sputter deposited onto different templates: **a** a smooth Si(001) wafer and **b** a Si(001) wafer covered by an alloy terminated $40 \times (2.5\,\text{nm}\,Si_{0.25}Ge_{0.75}/10\,\text{nm}\,Si)$ multilayer film with a self-organized array of {105} faceted SiGe pyramids (see Fig. 5). All scans are recorded with samples oriented azimuthally such that the [100] direction is parallel to the plane of incidence. The scans are normalized at $\Omega = 0$. The *insets* represent 1 µm × 1 µm AFM images of the corresponding film morphologies, color scale range: 10 nm (**a**) and 30 nm (**b**)

at the interface where the atoms are poorly coupled to the bulk magnetization. The magnetic moments of these atoms are not able to follow the magnetization reversal, and thus effectively do not contribute to the magnetic roughness. Thus, the magnetic roughness is smoother and has a larger lateral correlation length than the structural roughness. On the {105}-faceted interface segments tilted by 11°, there is obviously a better coupling of the magnetic moments at the Co interface to those in the bulk, as is sketched in Fig. 10b. This picture also agrees with the finding that the structural interfaces in the sandwich grown on the smooth substrate are more jagged than the ones on the patterned templates [9]. In a theoretical investigation it has indeed been revealed that the magnetization of random surfaces is more reduced than that of nanofaceted ones [74].

4.2 *Magnetic anisotropy*

Besides magnetic roughness, self-organized semiconductor templates also allow the systematic study of magnetic anisotropy as a function of the template symmetry. Here,

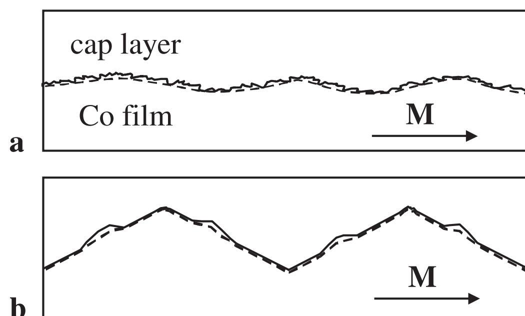

FIGURE 10 Sketch of the structural interface (*solid line*) and the magnetic boundary (*dashed line*) of a magnetic thin film with bulk magnetization ***M***. **a** Film with random interfacial roughness: The sharp asperities do not contribute to the magnetic interface resulting in a larger lateral correlation length and a reduced rms value of the magnetic roughness. **b** Nanofaceted film: The structural and the magnetic interface are nearly identical. The *vertical scales* are exaggerated for better visibility of the different interfaces in both schemes

preliminary results of in-plane MOKE measurements are presented using templates that just match the symmetries illustrated in Fig. 1. In Fig. 11, hysteresis loops are shown for a 2-nm Cu/2-nm Co/2-nm Cu film deposited on the rippled SiGe surface shown in Fig. 4. There is a rectangular-shaped loop when applying the magnetic field along the ripples (Fig. 11a) and an *s*-shaped loop with field direction perpendicular to the ripples. In the latter case, the squareness M_R/M_S (derived from the ratio ω_0/ω_S of the Kerr signals at zero magnetic field and in saturation, respectively) decreases to about 0.6. In other words, the 70-nm-rippled template causes a uniaxial in-plane anisotropy of the 2-nm Co film with the easy axis of magnetization parallel to the ripples. In the second example, the same sandwich is deposited onto a close-packed array of four-sided {105}-faceted pyramids (see Fig. 5). Figure 12 shows the squareness of the hysteresis loops as a function of the azimuthal sample orientation. Here, a slight fourfold anisotropy is observed. The easy axes are along the ⟨100⟩ directions, i.e. parallel to the base edges of the pyramids, and the hard axes are along the ⟨110⟩ directions. Contrary to this, the ordered chains of hut crystallites [15, 26] mentioned in Sect. 4.1 caused a uniaxial anisotropy with the easy axis parallel to the long base edges of the crystallites.

5 Fabrication of nanomagnet arrays

Driven by the efforts of the magnetic recording industry to fabricate ultrahigh-density storage devices, fabrication and characterization of magnetic nanostructures, also called nanomagnets, become crucial. In the search for effective and inexpensive ways to fabricate large-area arrays of magnetic nanostructures, a variety of self-organization phenomena are explored as technologically simple alternatives with respect to man-made techniques (see recent reviews such as [13, 14]). Here, we propose the application of grazing-incidence deposition of magnetic material onto self-organized nanofaceted semiconductor surfaces, where shadowing results in the deposition of selected facets only. For this purpose, the templates have to fulfil certain requirements [9]. First, structure size and periodicity should be sufficiently small to yield a high density of nanomagnets. Second and

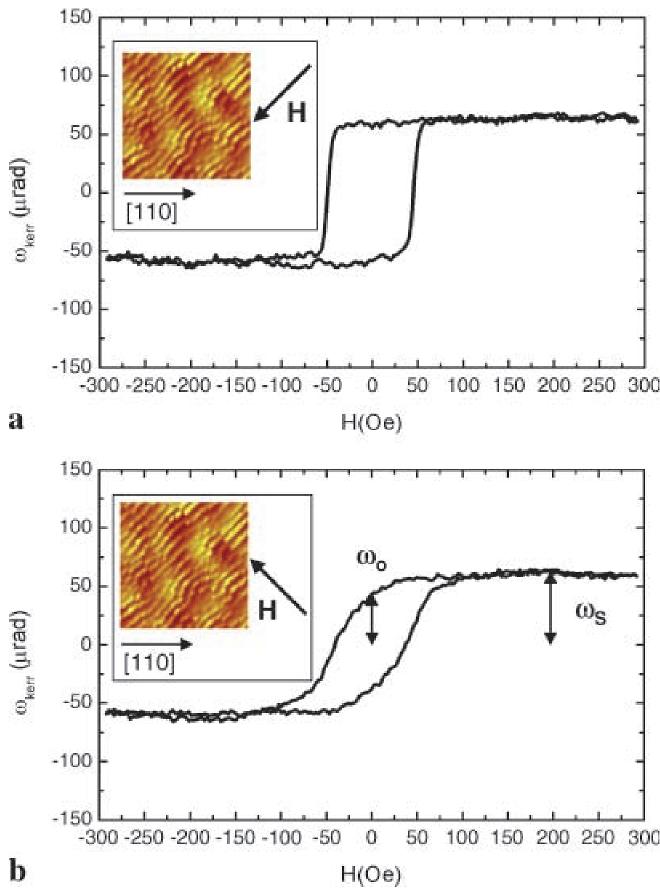

FIGURE 11 In-plane hysteresis loops measured by longitudinal MOKE for a 2 nm Cu/2 nm Co/2 nm Cu film grown by pulsed laser deposition on the step bunched SiGe template presented in Fig. 4. Hysteresis loops are measured in $[0\bar{1}0]$ (**a**) and $[\bar{1}00]$ (**b**) orientations. In **b** the Kerr signal at zero magnetic field, ω_o, and the Kerr signal in saturation, ω_S, are indicated. The *insets* with 1 µm × 1 µm AFM images of the template illustrate the corresponding orientation of the magnetic field with respect to the ripples

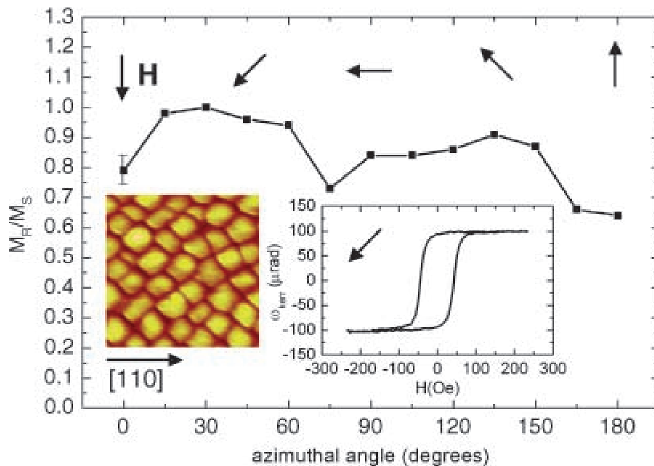

FIGURE 12 Squareness (M_R/M_S) of the hysteresis loops for an 2 nm Cu/2 nm Co/2 nm Cu sandwich grown by pulsed laser deposition on the regular array of four-sided pyramids of the SiGe film presented in Fig. 5. The *left inset* is a 1 µm × 1 µm AFM image of the surface of the Co film, color scale range: 20 nm. *Arrows* are shown to identify the orientation of the magnetic field with respect to the pyramids for a given azimuthal angle φ. The *right inset* shows the hysteresis loop for the $[0\bar{1}0]$ orientation

equally important, the facet structure of the template should be such that the resulting nanomagnets are separated from each other. An ideal candidate for fabricating isolated nanomagnets would be a template that exhibits just three types of nanofacets, because this allows the exclusive coverage of one selected facet type under grazing-incidence deposition. The {100}-faceted NaCl(111) surface [75] and NaCl thin films grown on Cu(211) [76] provide such a morphology; indeed, {100}-faceted NaCl(111) has been used as a template for shadow deposition of Fe [77]. However, from an applications point of view, sodium chloride as a substrate material has severe disadvantages. A native-oxide-covered $Si_{1-x}Ge_x$ film grown on the technologically most relevant Si(001) substrate is much more promising in this respect. Figure 13 presents such a nanofaceted surface that originates from a strain-driven step-bunch-to-facet transition [26] occurring in a 2.5-nm $Si_{0.55}Ge_{0.45}$ film grown on Si(001) with a 4° miscut towards $[\bar{1}\bar{1}0]$. It shows a distinct zigzag structure (Fig. 13a). The polar plot of the histogram of orientations of local surface normals (inset of Fig. 13a) reveals the existence of $\{\bar{1}05\}$ and $\{0\bar{1}5\}$ facets and (001) terraces. By transforming the three peaks of the histogram back into a topography image, we found that the $(\bar{1}05)$ and $(0\bar{1}5)$ facets are surprisingly uniform parallelograms with short edges of about 25 nm and long edges of 35 nm, and an acute angle of 47° (Fig. 13b). They form chevron-like chains. Their areal density is about $0.25 \times 10^{12}/\text{in}^2$. The (001) facets are predominantly squares with a size of 35 nm by 35 nm. The facets form a close-packed array, causing the observed size uniformity. Figure 13b shows a 3D model of the ideal nanofacet arrangement [15]. It reminds us of a pattern frequently used by M.C. Escher to pretend three-dimensionality. Here, however, the pattern is indeed three dimensional, and deposition geometries can be realized that result in an exclusive covering of one type of the parallelogram-shaped {105} facets. Figure 13c shows a scanning electron (SEM) image of a shadow-deposited 2-nm Co/2-nm Cu double layer [11]. It exhibits bright patches that are identified as the Co-covered $(\bar{1}05)$ nanofacets [11], while the continuously deposited crosscheck sample does not show any distinct contrast in SEM. The area fraction of the bright patches is 0.25 ± 0.02, which is in excellent agreement with the surface coverage one would expect from the model presented in Fig. 13b.

Figure 14 shows MOKE hysteresis loops for selected sample orientations of both the shadow-deposited sample and the continuous film, whereas the squareness versus the azimuthal orientation of the external field is plotted in Fig. 15. In order to increase the Kerr signal of the shadow-deposited sample, the thickness of the Co film was increased to about 5 nm [11]. There are two significant differences between the two samples. Firstly, the shadow-deposited film reveals saturation fields in the range of kOe, which is ten-times higher than the fields observed for the homogeneous film. Secondly and most importantly, there is a change in the magnetic anisotropy. The nanostructured ferromagnets exhibit a strong uniaxial anisotropy. Along the $[\bar{1}00]$ direction, an *s*-shaped hysteresis is found with almost vanishing remanence, whereas the easy axis of magnetization is in [010], i.e. parallel to the long edges of the $(\bar{1}05)$ facets. In Fig. 15a, the theoretical dependence for an ideal uniaxial behavior normalized to the max-

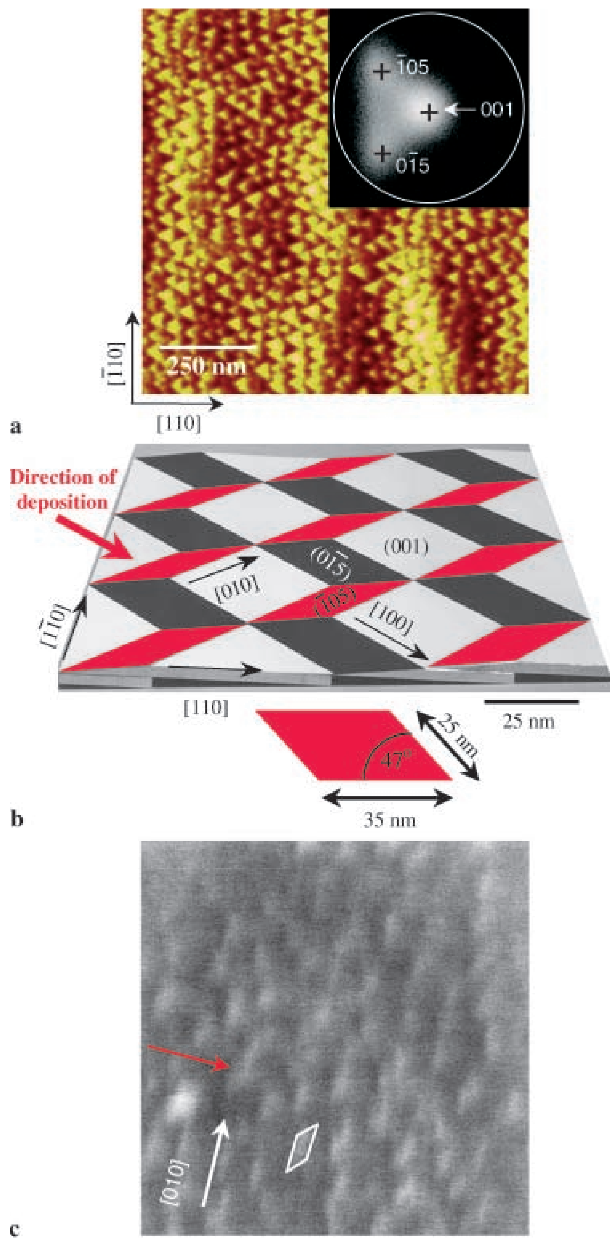

FIGURE 13 Fabrication of large-area nanomagnet arrays by shadow deposition of magnetic material onto a self-organized semiconductor template. **a** 1 µm × 1 µm AFM image of a 2.5 nm $Si_{0.55}Ge_{0.45}$ film grown on vicinal Si(001) substrate with a 4° miscut towards [$\bar{1}\bar{1}0$], color scale range is 5 nm, *inset*: 2D histogram of the orientations of local surface normals calculated from the image after correction for the substrate miscut. The histogram is displayed as a polar plot, with the white circle marking a polar angle of 15°. It reveals the existence of (001), ($\bar{1}05$), and ($0\bar{1}5$) facets. **b** 3D model of the ideal facet arrangement (to scale). The (001) facets (white) are square shaped with 35 nm long edges parallel to ⟨100⟩. The ($\bar{1}05$) and ($0\bar{1}5$) facets are parallelograms that are arranged in a chevron array. If this surface is shadow deposited under the direction indicated by the *red arrow* only the ($\bar{1}05$) facets (*red*) are coated. Their dimensions are indicated in the sketch below the model. **c** 360 nm × 360 nm SEM images of the template shown in **a** after shadow deposition of a 2 nm Co/2 nm Cu double layer. The *red arrow* denotes the (projected) orientation of the evaporation and the white parallelogram denotes size and orientation of the ($\bar{1}05$) facets

imum of the experimental results is also given. The continuous film (Fig. 15d) has nearly isotropic magnetic behavior, although some uniaxial contribution can be identified with easy and hard axes along [110] and [$\bar{1}10$], respectively [11].

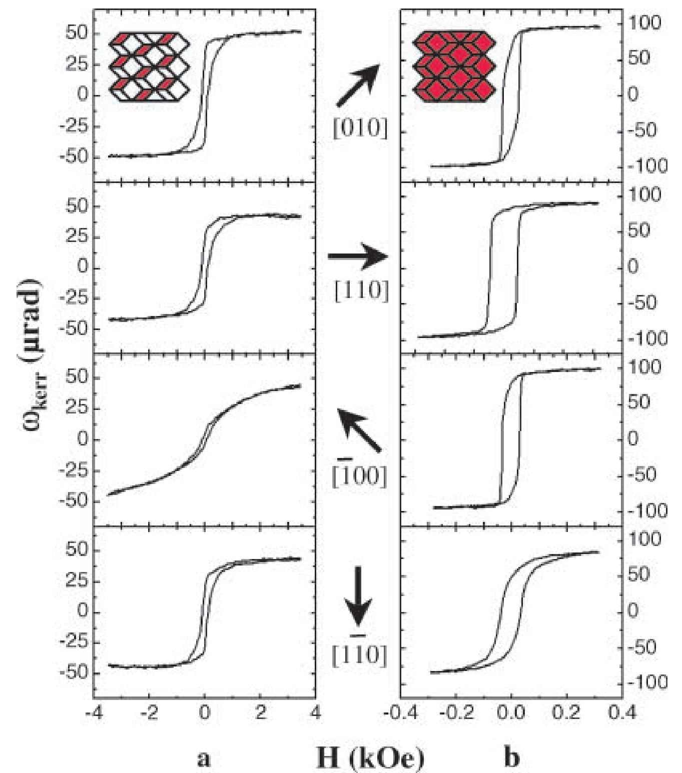

FIGURE 14 Longitudinal MOKE hysteresis loops measured in ⟨100⟩ and ⟨110⟩ orientations for shadow deposition and normal incidence deposition onto the nanofaceted template shown in Fig. 13a,b. **a** Shadow deposition of 5 nm Co onto the Cu covered ($\bar{1}05$) facets. **b** Continuous 2 nm thick Co film prepared by normal incidence deposition. *Arrows* and *insets* are shown to identify the orientation of the magnetic field with respect to the nanostructures for a given azimuthal angle φ. Note the different scales for the magnetic field in **a** and **b**

The strong increase in the saturation field H_s for the shadow-deposited film indicates that the creation of reversed domains, and thus domain walls, is impossible due to the small lateral size of the individual nanomagnets. Thus, one has to assume the magnetization reversal by rotation [78], which usually happens at higher fields. Summarizing, the MOKE results indicate the existence of a large-area array of highly ordered ferromagnetic nanostructures that show uniaxial in-plane anisotropy and are probably single-domain nanomagnets. The obtained areal density is $0.25 \times 10^{12}/\text{in}^2$ predefined by the facet arrangement of the template. The nanomagnet base size, however, can be tuned from the entire facet size to a smaller size by further reducing the polar angle of incidence and varying the azimuthal angle. The example demonstrates that shadow deposition of magnetic material on nanofaceted, self-organized semiconductor substrates is an efficient way of fabricating ultrahigh-density nanomagnet arrays. The SiGe self-organized templates bear the potential of being easily implemented in mainstream semiconductor technology. However, it is doubtful that the degree of self organization can be increased so far that the nanomagnet density achieved above can be fully utilized in non-volatile storage devices such as magnetic random access memories [79]. Instead, applications are imaginable that do not rely on ideal periodicity, such as artificial vortex pinning in superconducting films [80].

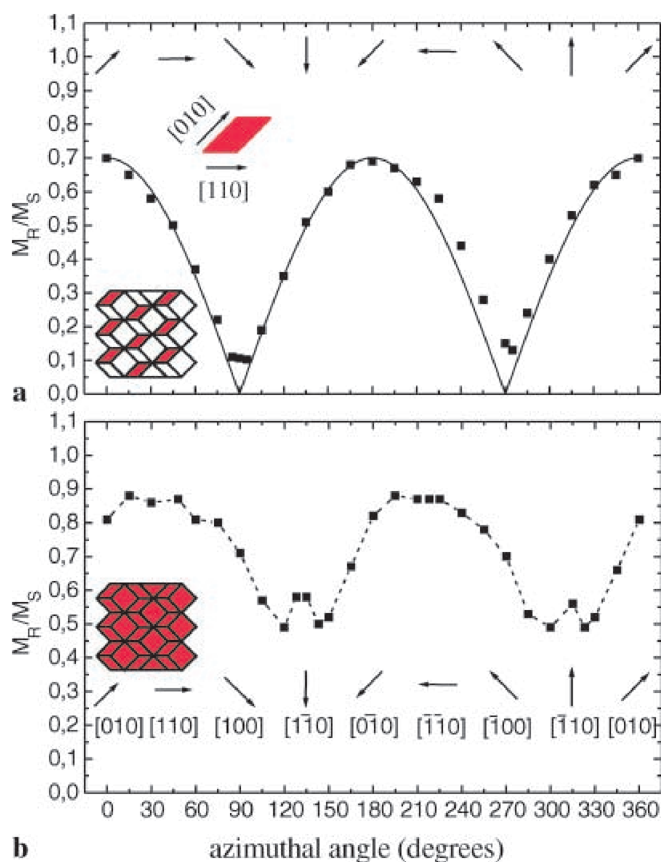

FIGURE 15 Squareness (M_R/M_S) of the hysteresis loops as a function of sample orientation with respect to the direction of magnetic field for the shadow deposited sample (**a**) and the continuous film (**b**). The *solid line* in **a** represents $|\cos(\varphi)|$ scaled to the maximum of M_R/M_S

6 Summary and outlook

Routes towards self-organized nanostructured semiconductor surfaces have been reviewed, with emphasis on nanostructure size, uniformity and pattern symmetry, i.e. evaluating their potential usability as templates for preparing nanostructured magnetic thin films. These films can be used to study fundamental aspects of magnetism at surfaces and interfaces. Finally, it was demonstrated that nanomagnet arrays with an areal density of $0.25 \times 10^{12}/\text{in}^2$ and surprising uniformity can be created by shadow deposition of self-organized nanofaceted semiconductor films. Using the patterns presented here, many more possible nanomagnet arrays are imaginable. One possibility is utilizing the different sticking probabilities of the various nanofacets. One can also imagine filling the pits of the checkerboard pattern (Fig. 6) or the ion-bombardment-induced dot arrays (Fig. 8) with magnetic material by preferential nucleation.

It should be noted that self-organized semiconductor surfaces may serve as templates for thin films of organic material as well, like self-assembled monolayers, organic crystallites and polymer films. Promising investigations have been started, for example, for protein adsorption on germanium nanopyramids [81]. Furthermore, it is thinkable to use self-organized semiconductor nanostructures as a stamp, like in nanoimprint technology [82], to transform the surface patterns of other materials, like polymers, that are subsequently used as nanopatterns themselves [83]. Utilizing self-organized semiconductor substrates, which is still an interesting subject of basic and applied research on its own, as templates to create nanostructures of other material classes is expected to support the exploration of novel physical phenomena in fields like nanomagnetism, organic semiconductors and nanocomposites.

ACKNOWLEDGEMENTS The results presented here have been obtained in collaboration with M.G. Lagally, J.F. MacKay, D.E. Savage and Y.H. Phang (University of Wisconsin-Madison), with J. Kirschner, H.P. Oepen, J. Barthel, M. Füting, S. Manoharan and W. Lutzke (Max Planck Institute of Microstructure Physics, Halle), and C. Hofer, M. Xu and P. Hosemann (Leoben). The author further wishes to thank L. Peticolas and J.C. Bean (Murray Hill), as well as K. Lyutovich and E. Kasper (Stuttgart), for growing the SiGe samples, and T. Bobeck, S. Facsko and H. Kurz (Aachen) for providing the ion-bombarded GaSb sample. Financial Support by the Fonds zur Förderung der wissenschaftlichen Forschung, Austria (Project No. P14009-TPH) is acknowledged.

REFERENCES

1 D.M. Eigler, E.K. Schweizer: Nature **344**, 524 (1990)
2 A.D. Kent, D.M. Shaw, S.V. Molnar, D.D. Awschalom: Science **262**, 1249 (1993)
3 M.I. Lutwyche, M. Despont, U. Drechsler, U. Dürig, W. Haberle, H. Rothuizen, R. Stutz, R. Widmer, G.K. Binnig, P. Vettiger: Appl. Phys. Lett. **77**, 3299 (2000)
4 S. Jakubith, H.H. Rotermund, W. Engel, A. von Oertzen, G. Ertl: Phys. Rev. Lett. **65**, 3013 (1990)
5 P. Zeppenfeld, M. Krzyzowski, C. Romainczuk, G. Comsa, M.G. Lagally: Phys. Rev. Lett. **72**, 2737 (1994)
6 V.A. Shchukin, D. Bimberg: Rev. Mod. Phys. **71**, 1125 (1999)
7 S. Facsko, T. Dekorsy, C. Koerdt, C. Trappe, H. Kurz, A. Vogt, H.L. Hartnagel: Science **285**, 1551 (1999)
8 V.A. Shchukin, D. Bimberg: Appl. Phys. A **67**, 687 (1998)
9 C. Teichert: Phys. Rep. **365**, 335 (2002)
10 D. Bimberg, M. Grundmann, N.N. Ledentsov: *Quantum Dot Heterostructures* (Wiley, Chichester 1999)
11 C. Teichert, J. Barthel, H.P. Oepen, J. Kirschner: Appl. Phys. Lett. **74**, 588 (1999)
12 Phys. Today **48**, 24 (April 1995)
13 H.P. Oepen, J. Kirschner: Current Opinion in Solid State and Materials, Science **4**, 217 (1999)
14 J. Shen, J. Kirschner: Surf. Sci. **500**, 300 (2002)
15 C. Teichert, J.C. Bean, M.G. Lagally: Appl. Phys. A **67**, 675 (1998)
16 J.F. MacKay, C. Teichert, D.E. Savage, M.G. Lagally: Phys. Rev. Lett. **77**, 3925 (1996)
17 H. Jenniches, M. Klaua, H. Höche, J. Kirschner: Appl. Phys. Lett. **69**, 3339 (1996)
18 D.J. Srolovitz: Acta Metall. **37**, 621 (1989)
19 E. Bauer: Z. Kristallogr. **110**, 372, 395 (1958)
20 D.J. Eaglesham, M. Cerullo: Phys. Rev. Lett. **64**, 1943 (1990)
21 Y.-W. Mo, M.G. Lagally: J. Cryst. Growth **111**, 876 (1991)
22 U. Köhler, O. Jusko, B. Müller, M. Horn-von Hoegen, M. Pook: Ultramicroscopy **42–44**, 832 (1992)
23 R. Butz, S. Kampers: Appl. Phys. Lett. **61**, 1307 (1992)
24 X. Chen, F. Wu, Z. Zhang, M.G. Lagally: Phys. Rev. Lett. **73**, 850 (1994)
25 Y.H. Phang, C. Teichert, M.G. Lagally, L.J. Peticolas, J.C. Bean, E. Kasper: Phys. Rev. B **50**, 14435 (1994)
26 C. Teichert, Y.H. Phang, L.J. Peticolas, J.C. Bean, M.G. Lagally: In: *Surface Diffusion: Atomistic and Collective Processes*, ed. by M.C. Tringides (Plenum Press, New York 1997) p. 297
27 J. Tersoff, Y.H. Phang, Z. Zhang, M.G. Lagally: Phys. Rev. Lett. **75**, 2730 (1995)
28 C. Schelling, G. Springholz, F. Schäffler: Thin Solid Films **380**, 20 (2000)
29 M. Mühlberger, C. Schelling, G. Springholz, F. Schäffler: Physica E **13**, 990 (2002)
30 J. Mysliveček, C. Schelling, G. Springholz, F. Schäffler, B. Voigtländer, P. Šmilauer: Mater. Sci. Eng. B **89**, 410 (2002)
31 C. Schelling, G. Springholz, F. Schäffler: Phys. Rev. Lett. **83**, 995(1999)

32 Y.W. Mo, D.E. Savage, B.S. Swartzentruber, M.G. Lagally: Phys. Rev. Lett. **65**, 1020 (1990)
33 Y. Fujikawa, K. Akiyama, T. Nagao, T. Sakurai, M.G. Lagally, T. Hashimoto, Y. Morikawa, K. Terakura: Phys. Rev. Lett. **88**, 176101 (2002)
34 C. Teichert, M.G. Lagally, L.J. Peticolas, J.C. Bean, J. Tersoff: Phys. Rev. B **53**, 16 334 (1996)
35 C. Teichert, J. Tersoff, M.G. Lagally: In: *Series on Directions in Condensed Matter Physics, vol. 14: Morphological Organization in Epitaxial Growth and Removal*, ed. by Z. Zhang, M.G. Lagally (World Scientific, Singapore 1998) p. 177
36 J. Tersoff, C. Teichert, M.G. Lagally: Phys. Rev. Lett. **76**, 1675 (1996)
37 Q. Xie, A. Madhukar, P. Chen, N.P. Kobayashi: Phys. Rev. Lett. **75**, 2542 (1995)
38 G. Springholz, V. Holy, M. Pinczolits, G. Bauer: Science **282**, 734 (1998)
39 G. Springholz, M. Pinczolits, P. Mayer, V. Holy, G. Bauer, H.H. Kang, L. Salamanca-Riba: Phys. Rev. Lett. **84**, 4669 (2000)
40 G. Medeiros-Ribeiro, A.M. Bratkovski, T.I. Kamins, D.A.A. Ohlberg, R.S. Wiliams: Science **279**, 353 (1998)
41 M.A. Lutz, R.M. Feenstra, P.M. Mooney, J. Tersoff, J.O. Chu: Surf. Sci. **316**, L1075 (1994)
42 F.M. Ross, R.M. Tromp, M.C. Reuter: Science **286**, 1931 (1999)
43 P. Politi, G. Grenet, A. Marty, A. Ponchet, J. Villain: Phys. Rep. **324**, 271 (2000)
44 D.E. Jesson, K.M. Chen, S.J. Pennycook, T. Thundat, R.J. Warmack: Science **268**, 1161 (1995)
45 S.Y. Shiryaev, F. Jensen, J.L. Hansen, J.W. Petersen, A.N. Larsen: Phys. Rev. Lett. **78**, 503 (1997)
46 Y.H. Xie, S.B. Samavedam, M. Bulsara, T.A. Langdo, E.A. Fitzgerald: Appl. Phys. Lett. **71**, 3567 (1997)
47 E. Kasper, K. Lyutovich, M. Bauer, M. Oehme: Thin Solid Films **336**, 319 (1998)
48 C. Teichert, C. Hofer, K. Lyutovich, M. Bauer, E. Kasper: Thin Solid Films **380**, 28 (2000)
49 M. Bauer, M. Oehme, K. Lyutovich, E. Kasper: Thin Solid Films **336**, 104 (1998)
50 F. Leroy, J. Eymery, P. Gentile, F. Fournel: Appl. Phys. Lett. **80**, 3078 (2002)
51 J. Dabrowski, H.J. Müssig: *Silicon Surfaces and Formation of Interfaces – Basic Science in the Industrial World* (World Scientific, Singapore 2000)
52 B. Voigtländer: Surf. Sci. Rep. **43**, 127 (2001)
53 R. Behrisch (Ed.): *Sputtering by Particle Bombardment I–II* (Springer, Berlin 1983)
54 S. Rusponi, C. Boragno, U. Valbusa: Phys. Rev. Lett. **78**, 2795 (1997)
55 E. Chason, T.M. Mayer, B.K. Kellermann, D.T. McIlroy, A.J. Howard: Phys. Rev. Lett. **72**, 3040 (1994)
56 R.M. Bradley, J.M.E. Harper: J. Vac. Sci. Technol. A **6**, 2390 (1988)
57 T. Michely, K.H. Besocke, G. Comsa: Surf. Sci. **230**, L135 (1990)
58 J.C. Girard, Y. Samson, S. Gauthier, S. Rousset, J. Klein: Surf. Sci. **302**, 73 (1994)
59 C. Teichert, C. Ammer, M. Klaua: Phys. Status Solidi A **146**, 223 (1994)
60 G. Costantini, S. Rusponi, R. Gianotti, C. Boragno, U. Valbusa: Surf. Sci. **416**, 245 (1998)
61 M. Ritter, M. Stindtmann, M. Farle, K. Baberschke: Surf. Sci. **348**, 243 (1996)
62 T. Bobeck, S. Facsko, H. Kurz, T. Dekorsy, M. Xu, C. Teichert: Phys. Rev. B, submitted
63 S. Facsko, T. Bobeck, H. Kurz, T. Dekorsy, S. Krysta, R. Kremer: Appl. Phys. Lett. **80**, 130 (2002)
64 S. Park, B. Kahng, H. Jeong, A.L. Barabási: Phys. Rev. Lett. **83**, 3486 (1999)
65 F. Frost, A. Schindler, F. Bigl: Phys. Rev. Lett. **85**, 4116 (2000)
66 R. Gago, L. Vázquez, R. Cuerno, M. Varela, C. Ballesteros, J.M. Albella: Appl. Phys. Lett. **78**, 3316 (2001)
67 Phys. Today **49**, 21 (November 1996)
68 J.B. Kortright, D.D. Awschalom, J. Stöhr, S.D. Bader, Y.U. Idzerda, S.S.P. Parkin, I.K. Schuller, H.C. Siegmann: J. Magn. Magn. Mater. **207**, 7 (1999)
69 G.H. Lander, J Magn. Magn. Mater. **242–245**, 3 (2002)
70 J.W. Freeland, V. Chakarian, K. Bussmann, Y.U. Idzerda, H. Wende, C.C. Kao: J. Appl. Phys. **83**, 6290 (1998)
71 J.J. Kelly, B.M. Barnes, F. Flack, D.P. Lagally, D.E. Savage, M. Friesen, M.G. Lagally: J. Appl. Phys. **91**, 9978 (2002)
72 J.B. Kortright, O. Hellwig, D.T. Margulies, E.E. Fullerton: J. Magn. Magn. Mater. **240**, 325 (2002)
73 R.M. Osgood III, S.K. Sinha, J.W. Freeland, Y.U. Idzerda, S.D. Bader: J. Appl. Phys. **85**, 4619 (1999)
74 D. Zhao, F. Liu, D.L. Huber, M.G. Lagally: Phys. Rev. B **62**, 11 316 (2000)
75 K.W. Keller: Metall. Trans. A **22**, 1299 (1991)
76 S. Fölsch, A. Helms, A. Riemann, J. Repp, G. Meyer, K.H. Rieder: Surf. Sci. **497**, 113 (2002)
77 A. Sugawara, G.G. Hembree, M.R. Scheinfein: J. Appl. Phys. **82**, 5662 (1997)
78 A. Aharoni: *Introduction to the Theory of Ferromagnetism* (Clarendon Press, Oxford 1996)
79 J.M. Daughton: Thin Solid Films **216**, 162 (1992)
80 J.I. Martin, M. Vélez, A. Hoffmann, I.K. Schuller, J.L. Vicent: Phys. Rev. Lett. **83**, 1022 (1999)
81 M. Riedel, B. Müller, E. Wintermantel: Biomater. **22**, 2307 (2001)
82 S.Y. Chou, P.R. Krauss, P.J. Renstrom: Appl. Phys. Lett. **67**, 3114 (1995)
83 H. Shi, W.B. Tsai, M.D. Garrison, S. Ferrari, B.D. Ratner: Nature **398**, 593 (1999)